World Electric Vehicle Journal

MDPI

Article

Diagnosis of Multiple Open-Circuit Faults in Three-Phase Induction Machine Drive Systems Based on Bidirectional Long Short-Term Memory Algorithm

Badii Gmati [1], Amine Ben Rhouma [1,2], Houda Meddeb [1] and Sejir Khojet El Khil [1,*]

[1] LR11ES15 Laboratoire des Systèmes Electriques, Ecole Nationale d'Ingénieurs de Tunis, Université de Tunis El Manar, 1002 Tunis, Tunisia; badii.gmati@enit.utm.tn (B.G.); amine.benrhouma@enit.rnu.tn (A.B.R.); meddebhouda@gmail.com (H.M.)
[2] Department of Electrical Engineering, ENSIT, Université de Tunis, 1008 Tunis, Tunisia
* Correspondence: sejir.kek@edu.isetcom.tn

Abstract: Availability and continuous operation under critical conditions are very important in electric machine drive systems. Such systems may suffer from several types of failures that affect the electric machine or the associated voltage source inverter. Therefore, fault diagnosis and fault tolerance are highly required. This paper presents a new robust deep learning-based approach to diagnose multiple open-circuit faults in three-phase, two-level voltage source inverters for induction-motor drive applications. The proposed approach uses fault-diagnosis variables obtained from the sigmoid transformation of the motor stator currents. The open-circuit fault-diagnosis variables are then introduced to a bidirectional long short-term memory algorithm to detect the faulty switch(es). Several simulation and experimental results are presented to show the proposed fault-diagnosis algorithm's effectiveness and robustness.

Keywords: open-circuit fault; induction motor; sigmoid function; bidirectional long short-term memory; deep learning

Citation: Gmati, B.; Ben Rhouma, A.; Meddeb, H.; Khojet El Khil, S. Diagnosis of Multiple Open-Circuit Faults in Three-Phase Induction Machine Drive Systems Based on Bidirectional Long Short-Term Memory Algorithm. *World Electr. Veh. J.* **2024**, *15*, 53. https://doi.org/10.3390/wevj15020053

Academic Editors: Diego Bellan and Jelena Loncarski

Received: 13 November 2023
Revised: 21 January 2024
Accepted: 30 January 2024
Published: 5 February 2024

1. Introduction

Three-phase pulse-width modulation (PWM) voltage source inverters (VSIs) have been widely used for grid-connected converters or AC machines' variable-speed drive applications. For most of these applications, high reliability and availability are of utmost importance. Consequently, the condition monitoring, fault detection, and fault tolerance of three-phase PWM VSIs are widely requested functions that should be added to the drive system's controller [1,2].

An open-circuit (OC) fault is one of the most relevant faults that may affect induction-motor variable-speed drives [3]. This type of fault may affect one or more power semiconductors. As discussed in [4,5], OC faults introduce severe perturbations: a DC current injection, an overcurrent, and pulsating electromagnetic torque. In some cases, the electric drive must be shut down. Consequently, fault diagnosis and fault tolerant control [5,6] are of utmost importance. Several studies have focused on OC faults, and different algorithms have been proposed, as summarized by many survey articles [1–3,7,8]. OC fault-diagnostics methods are mainly classified as model-based approaches [9–21], signal-based approaches [22–30], and data-driven approaches [31–41].

Model-based fault-diagnosis approaches use the mathematical model of the electric machine and/or the model of the voltage source inverter. The main idea is to compare estimated quantities obtained from the system's model to the measured quantities. In most cases, electric machine currents [9–14] and output voltages of the voltage source inverter [15–20] are the estimated quantities.

In a well-functioning operation, the measured and estimated quantities are almost the same. Hence, the estimation error converges to zero. When an open-circuit fault is affecting one or more power switch(es), the deviation of the estimation error is used to detect the fault and to identify the faulty switch(es).

In [9,10], Jlassi et al. use the current form factor (CFF) to detect open-circuit faults in permanent magnet synchronous machine (PMSM) drives for both generator and motor applications. The main idea is to compare the CFF obtained from the measured currents to the CFF obtained from estimated currents based on the state Luenberger observer. A similar approach is discussed in [11] to detect current sensors and open-circuit faults in grid-connected three-level NPC inverters. In this study, the currents are estimated using a sliding-mode observer.

The current residual approach is proposed to diagnose open-circuit faults in PMSM, and induction-motor drive systems are discussed in [12,13], respectively.

Voltage-based OC fault detection has been discussed in [15–20]. To avoid the use of additional voltage sensors, which may increase the system's cost, the output voltage of the VSI should be estimated. In [15], an OC fault-diagnosis scheme is proposed based on voltage estimation for an induction machine drive system. A state estimator is used to estimate the phase voltage based on the induction machine model. The estimated voltage is compared to the voltage obtained from the DC-link voltage and the inverter switching signals. The residual of the estimation error is used to detect the faulty switch(es). Nevertheless, this approach needs the use of low-pass filters that require high tuning and introduce delays in the detection time. Freire et al. present a similar approach applied to PMSM drive systems [16]. In [17], the calculated common-mode voltage behavior is used to detect and locate OC faults in three-phase, two-level inverters for induction machine drive systems.

Recently, with the increase in the use of model predictive control (MPC) in variable-speed drive systems, some studies propose the use of motor-current prediction errors to detect OC faults for PMSM drive systems [22–25]. Thanks to the robustness of MPC, the motor-current prediction errors are very low in well-functioning (healthy) operation modes. It has been shown that in the case of OC faults, the motor-current prediction errors increase, allowing for the detection and identification of the fault switch [22–25].

Signal-based methods typically involve motor-current signature analysis [26–30]. In [26], a single current sensor is employed to detect OS faults in the PMSM drive system. A DC-link current sensor is used to reconstruct the motor stator currents. Then, the normalized average value of the reconstructed current is used to detect the faulty switch. Sejir et al. [27] present a current analysis-based algorithm to detect OS faults in PMSM drive systems. The fault-detection variables use the interaction between two stator currents, which allows for the detection of 27 types of OC faults and current-sensor faults. Reference current errors are adopted to detect OC faults in voltage source inverters [28]. However, this approach can only be used for closed-loop controlled electric drives.

More recently, data-driven fault-diagnosis approaches have become more attractive for fault-diagnosis and fault-classification purposes [31–41]. Indeed, data-driven approaches are only based on recorded data obtained from measured quantities, instead of specific complex mathematical models.

In [31,32], a Fast Fourier Transform (FFT) algorithm is used to extract open-circuit fault features from motor currents [31] or the inverter's output line-to-line voltage [32]. Then, a fast-learning technology is applied to diagnose the faulty switch(es). Xia et al. [33] present a transferrable data-driven algorithm for open-circuit switch-fault diagnosis in three-phase inverters. A deep learning-based approach for the open switch-fault diagnosis of three-phase PWM converters is discussed in [34]. Current behaviors in healthy and faulty operation modes are analyzed for fault feature extraction. Hang et al. [36] propose an OC fault-diagnosis algorithm for PMSM drives using a wavelet convolutional neural network (WCNN). The normalized current vector trajectory graph obtained by the Clark transform is sent to the WCNN model to detect and localize the faulty power semi-conductor. However, this method

requires high-computation execution time and needs preprocessing for noise robustness. In [37], the online data-driven fault diagnosis of dual three-phase PMSM drives is discussed.

Long short-term memory networks (LSTMs) have been investigated for fault-diagnosis issues due to their high accuracy compared to other fault-diagnosis techniques [38–45]. The effectiveness of the method is confirmed in [38], where it is used to detect multiple open-circuit switch faults of the back-to-back converter in doubly fed induction generator (DFIG)-based wind turbine systems. A similar approach has been used to diagnose OC faults in multilevel converters [39–41]. The LSTM approach is applied for diagnosing faults in electric vehicles [42,43] and for motor electrical faults [44] and mechanical fault diagnosis [45].

A state-of-the-art review has shown that model-based OC fault-detection approaches are effective. However, these approaches need a good knowledge of the studied system's model. Furthermore, they are sensitive to the variations in the system's parameters. Moreover, they need a robust fault-detection threshold, which makes them complicated to elaborate. Signal-based OC fault-detection methods present a good alternative to model-based ones. They are attractive especially since they do not require either highly computational resources or extra hardware. Data-driven approaches have the advantage of being only dependable on recorded data obtained from measured quantities instead of specific complex mathematical models. The main concerns of such algorithms are their complexity and the need for large-scale data for feature extraction, training, and validation. These requirements make real-time implementation difficult.

Therefore, by combining signal-based methods with those based on data, this scheme may achieve high-accuracy fault detection and fault localization results. Consequently, this paper proposes a bidirectional long short-term memory (BiLSTM)-based algorithm to diagnose open-circuit power semi-conductor faults in a three-phase PWM voltage source inverter for an induction-motor drive system. The main contribution of the proposed approach can be summarized as follows:

- √ The proposed method can achieve an accurate diagnosis of single and multiple open-circuit faults without any extra hardware requirements. Only already measured induction-motor stator currents are used.
- √ A new, robust current-normalization approach is developed to keep the motor currents free from load-torque and motor-speed transient variations.
- √ The normalized currents are then combined in order to generate three OC fault indicators. Then, the fault-detection variables are introduced to a BiLSTM network to identify the faulty switch(es). The BiLSTM network does not need to set any fault-detection threshold, which increases the accuracy and the effectiveness of the proposed approach.

The rest of the paper is organized as follows: Section 2 presents the fault-detection variables and analysis of the fault features. Section 3 describes the BiLSTM network and the fault-diagnosis algorithm. The performance of the proposed OC fault-diagnosis algorithm is analyzed through simulations in Section 4 and evaluated through experiments in Section 5. Finally, conclusions are drawn in Section 6.

2. Fault Features Analysis

The structure of the three-phase induction-motor drive system is depicted in Figure 1. The two-level VSI is composed of six IGBTs ($T_1 \rightarrow T_6$) and their anti-parallel diodes. Under healthy operation conditions, the induction-motor stator currents are expressed as:

$$\begin{cases} i_a(t) = I_m \sin(\omega t) \\ i_b(t) = I_m \sin(\omega t - \frac{2\pi}{3}) \\ i_c(t) = I_m \sin(\omega t - \frac{4\pi}{3}) \end{cases} \quad (1)$$

where I_m is the induction-motor stator current amplitude and ω is the synchronous electrical pulsation.

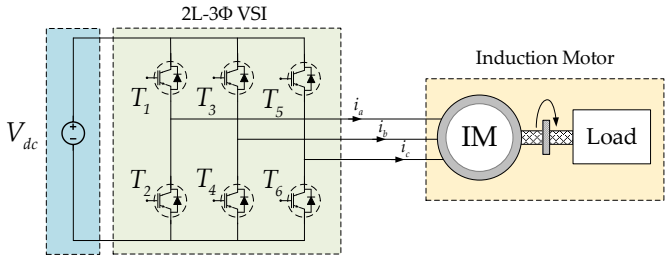

Figure 1. Structure of 2L-3Φ VSI-fed IM system.

When an open-circuit fault occurs, it produces a distortion of the stator currents with an increase in their amplitude, electromagnetic torque oscillations, and excess heat, which can lead to motor failures [27].

The motor currents can provide accurate signatures to ensure an effective diagnosis of OC faults. However, motor currents are sensitive to the load torque and motor-speed variations. To reduce the dependency of the OC fault signatures on load-torque and/or motor-speed variations, it is necessary to normalize the motor currents. In this way, several approaches discussed in the literature have been proposed as normalization tools: Park's vector modulus $\left\|i_{dq}\right\| = \sqrt{i_d^2 + i_q^2}$ in [23], the maximum absolute value of the motor-phase currents $\max\{|i_a|, |i_b|, |i_c|\}$ in [27], and the average absolute values of the motor-phase currents $\langle |i_n| \rangle_{n=\{a,b,c\}}$ in [28]. Although these methods provide good results, they also require additional computational effort and prior knowledge of the motor parameters to ensure a real-time normalization of diagnosis variables, which increases computation time and decreases the performance of the OC fault methods.

In this work, a new motor current-normalization approach is introduced. The main idea consists of applying the sigmoid function to the motor currents for the normalization process. The sigmoid function of the real variable x, $F(x)$, is defined as:

$$F(x) = \frac{2}{1 + e^{-\lambda x}} - 1 \tag{2}$$

where λ is a positive real. In Figure 2, the sigmoid function of the sinusoidal variable x is presented. It can be seen that $F(x)$ varies by ± 1 and has the same period as the variable x, apart from its maximum value x_m. The impact of the positive real λ on the dynamic of $F(x)$ is depicted in Figure 2. A greater λ value is higher and more $F(x)$ variation is faster.

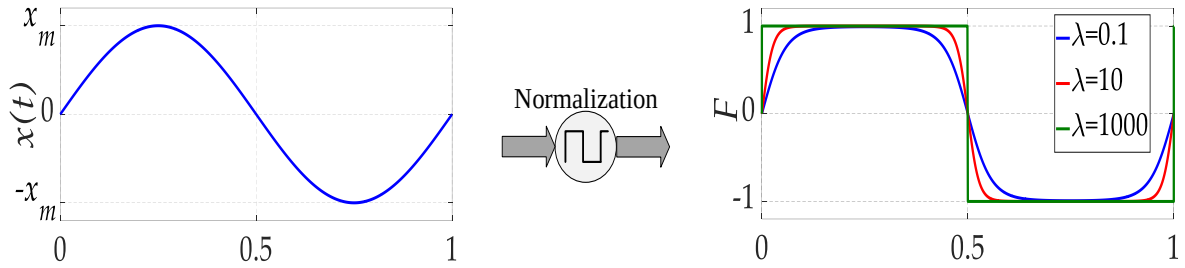

Figure 2. Sigmoid function for different coefficient values λ.

However, the motor currents do not have a pure sine waveform due to the impact of sampling, PWM, and measurement noises. As a result, the chattering problem appears in the normalized function and can be seen during the zero crossing of the current signal, as shown in Figure 3a.

To analyze this feature, the positive-current half-period is taken as an example. The current can be divided into a chattering zone, where the current is small, and a non-chattering area, due to an adequate current drop. The oscillations of the sigmoid function due to the chattering zone reduce the performance of the motor current-normalization approach. To

fix this issue and to reduce the chattering effect of the sigmoid function, the normalization function of the induction-motor stator current is modified; this is expressed below:

$$F(x) = \begin{cases} 0 & if \quad x \in [-x_h, x_h] \\ \frac{2}{1+e^{-\lambda x}} - 1 & else \end{cases} \tag{3}$$

where x_h is the minimum value of signal $x(t)$ that avoids the chattering problem. Figure 3b shows the output of the modified normalization function, where it is forced to be zero during the zero-crossing of the current signal. It should be noticed that, when the fault occurs in the non-chattering zone $[t_3; t_4]$, it can be immediately detected. However, if it occurs when $|x(t)| \leq x_h$, $[t_1; t_2]$, it cannot be detected, and we should wait for the next cycle.

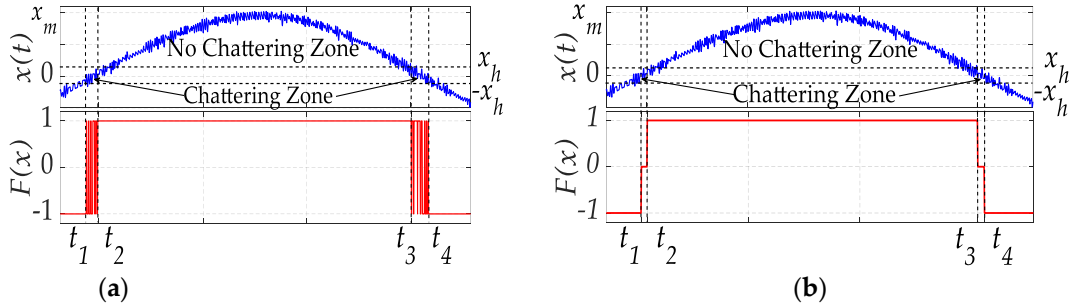

Figure 3. Current-normalization method: (**a**) with chattering problem, (**b**) without chattering problem.

By applying Equation (3) to the induction-motor stator currents, we obtain the variations of the sigmoid variables F_a, F_b and F_c of the motor currents i_a, i_b and i_c, respectively, as presented in Figure 4a. It can be seen that F_a, F_b and F_c have the same period as their corresponding motor currents and vary by ± 1, which makes them free from load-torque variations and motor-speed transient variations. Thereafter, three fault-diagnosis indictors—χ_a, χ_b and χ_c—are defined as follows:

$$\begin{cases} \chi_a = 2F_a - F_b - F_c \\ \chi_b = 2F_b - F_c - F_a \\ \chi_c = 2F_c - F_a - F_b \end{cases} \tag{4}$$

The variations in the fault-diagnosis indicators for one period of motor currents are depicted in Figure 4b. During the healthy mode of the induction-motor drive, the fault-detection variables exhibit similar behavior to the motor stator currents with the same period, and there is a phase shift between them equal to $2\pi/3$. Moreover, they vary by ± 4. It should be noted that the variations in the fault-detection variables are also independent of motor speed or load torque.

When an open-switch fault occurs, it affects the stator currents waveforms, as well as the F_a, F_b and F_c and χ_a, χ_b and χ_c waveforms. Figure 5a describes the stator currents and variations in the detection variables χ_a, χ_b and χ_c in the case of an open-switch fault of IGBT T_1 applied at time $t = 0.6$ s. Instantly, the behavior of χ_a, χ_b and χ_c is not the same as in the healthy operation mode. Indeed, χ_a loses its positive sequence, whereas χ_b and χ_c vary between 4 and -3.

A similar analysis was conducted for an open-switch fault of T_1 and T_2 applied at time $t = 0.6$ s, (open phase fault), as presented in Figure 5b. χ_a becomes equal to 0, and χ_b and χ_c are opposite and vary between 3 and -3. A third fault case is analyzed considering an open-switch fault of T_1 and T_4, as shown in Figure 5c. In this case, χ_a loses its positive sequence, χ_b loses its negative sequence, and χ_c varies between 3 and -3. The analysis of these three faults scenarios has shown for each open-switch fault that the detection variables $\chi_{a,b,c}$ have a specific feature. This feature makes them suitable to be used to

achieve a robust and reliable open-switch fault-detection algorithm for the studied electric drive system.

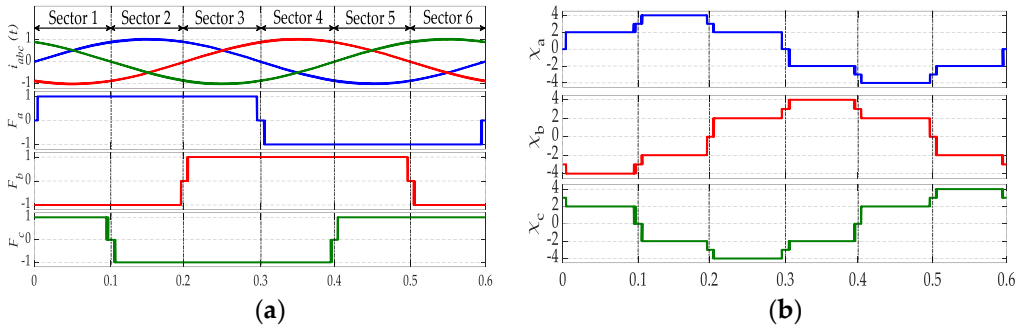

Figure 4. Time-domain waveforms of: (**a**) three-phase currents and sigmoid functions, (**b**) detection fault variables in healthy mode.

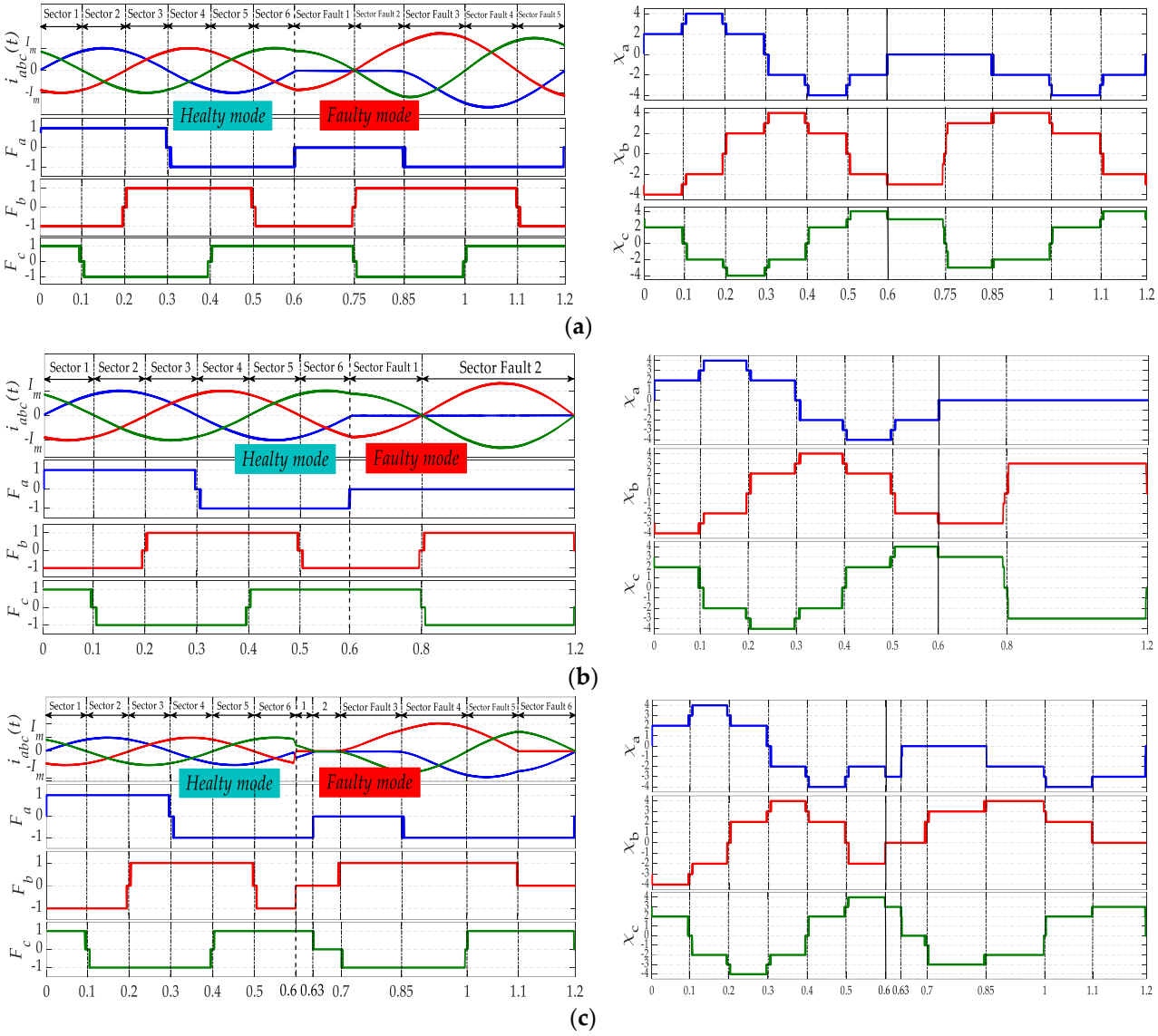

Figure 5. Time-domain waveforms of three-phase currents, sigmoid functions and detection fault variables for: (**a**) Fault in T_1, (**b**) Fault in T_1 and T_2, (**c**) Fault in T_1 and T_4.

3. LSTM Approach for Fault Diagnosis

3.1. LSTM Structure

LSTM is an improved version of a recurrent neural network (RNN), which has achieved satisfactory performance in sequence learning and temporal modeling [38].

LSTM has a special structure, which allows for solving the challenge of gradient vanishing or explosion in a simple RNN since it replaces the iterative transformation with addition in the calculation of hidden state [45]. The structure of an LSTM unit is illustrated in Figure 6.

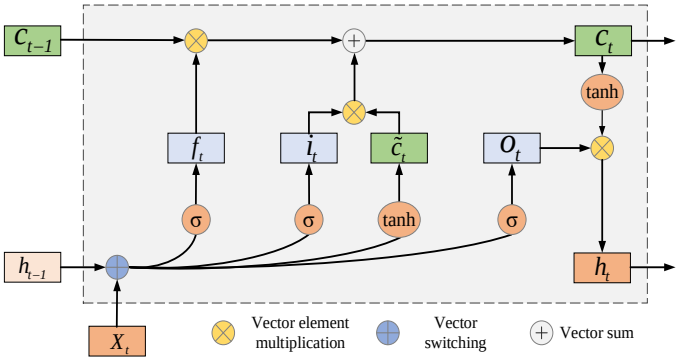

Figure 6. LSTM Network structure.

LSTM mainly consists of three gates: a forget gate f_t, an input gate i_t, and an output gate o_t. The forget-gate layer f_t determines which information should be forgotten. The equation of the forget-gate layer can be expressed as:

$$f_t = \sigma(w_f.[h_{t-1}, X_t] + b_f) \tag{5}$$

where X_t and h_{t-1} represent, respectively, the input at the current time and the output at the previous time of the LSTM network. W_f and b_f represent the weight and the bias of the forget-gate layer. σ is the sigmoid function and [ ] represents the concatenate operation.

The input-gate layer i_t updates the cell state based on the input at the current time X_t and the output at the previous time h_{t-1}. The equations of the input gate can be described as:

$$i_t = \sigma(w_i.[h_{t-1}, X_t] + b_i) \tag{6}$$

$$\widetilde{c}_t = \tanh(w_c.[h_{t-1}, X_t] + b_c) \tag{7}$$

where X_t and h_{t-1} represent, respectively, the input at the current time and the output at a previous time. W_i and b_i are the weight and the bias of the sigmoid function in the input-gate layer. tanh is a hyperbolic tangent function, W_c and b_c are the weight and the bias of the tanh function in the input-gate layer.

The output-gate layer o_t selects information that should be the next output, which depends on the cell state c_t. The equation of the output-gate layer can be expressed as Equation (8); w_o and b_o are the weight and the bias of the output-gate layer.

$$o_t = \sigma(w_o.[h_{t-1}, X_t] + b_o) \tag{8}$$

The cell state and the output (hidden) state at time step t are described by the following equations:

$$c_t = f_t \times c_{t-1} + i_t \times \widetilde{c}_t \tag{9}$$

$$h_t = \tanh(c_t) \times o_t \tag{10}$$

3.2. Stacked LSTM (MLSTM)

A stacked LSTM is a deep LSTM that consists of multiple LSTM layers, where each layer contains multiple memory cells. The inputs of the first LSTM layer are the sequence data, and the input of other LSTM layers is the hidden state of the previous LSTM layer. Therefore, the stacked LSTM hidden layers make the model deeper and more accurate. This type of network becomes a powerful method for challenging sequence prediction problems. The structure of a stacked LSTM with n hidden layers is shown in Figure 7.

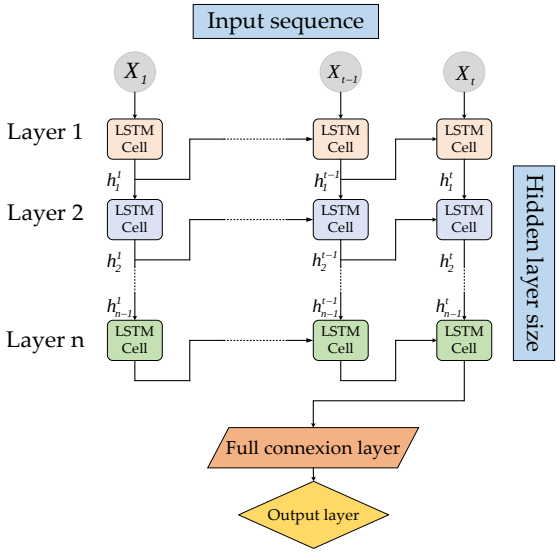

Figure 7. Stacked LSTM structure.

3.3. Bidirectional LSTMs (BiLSTM)

BILSTM is an emerging approach to address fault-diagnosis problems [46–50]. This technique has been shown to provide more accurate results than other classical methods and LSTM [50,51]. In this study, the BiLSTM network is used to identify and locate multiple open-circuit faults in a three-phase, two-level voltage source inverter for an induction-motor drive system. Compared with LSTM, BiLSTM can procure information from both earlier and later segments in sequence [51]. The BiLSTM structure consists of a forward LSTM layer and a backward LSTM layer, which reverses the direction of the input sequence flow [51,52]. Applying the LSTM twice makes the prediction results more integrated and leads to improving the accuracy of the model. Furthermore, it should be mentioned that BiLSTM is a much slower model and requires more time for training. The BiLSTM architecture is presented in Figure 8.

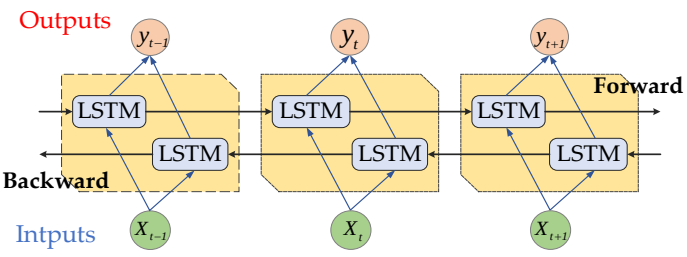

Figure 8. BiLSTM structure.

3.4. Evaluation Metrics

After building prediction models, several metrics can be used to evaluate the performance of models and compare them.

3.4.1. Root-Mean-Square Error (RMSE)

The root-mean-square error (RMSE) is the most commonly used performance measure for prediction tasks. The RMSE can be calculated by using (11).

$$RMSE = \sqrt{\frac{1}{n}\sum_{i=1}^{n}(y_i - \hat{y}_i)^2} \tag{11}$$

where $\hat{y}_i$ and y_i are the prediction and the real output value, and n is the number of data.

3.4.2. Mean Absolute Error (MAE)

The MAE is the other criterion used to evaluate the model performance. The MAE is expressed as (12).

$$MAE = \frac{1}{n}\sum_{i=1}^{n}|y_i - \hat{y}_i| \tag{12}$$

3.4.3. Mean Absolute Percentage Error (MAPE)

The MAPE is one of the most common metrics used to measure the prediction accuracy of a model and it is described as (13).

$$MPAE(\%) = \frac{1}{n}\sum_{i=1}^{n}\frac{|y_i - \hat{y}_i|}{y_i} \times 100 \tag{13}$$

The summation ignores observations where $y_i = 0$. In general, the lower the MAPE value is, the more accurate the model is.

The last metric used in this paper to evaluate the performance of the proposed algorithm is the accuracy of the prediction model, which is expressed as:

$$Accuracy(\%) = 100 - MPAE \tag{14}$$

3.5. Diagnostic Network Implementation and Validation

The proposed diagnosis method consists of the BiLSTM network with one hidden layer. The BiLSTM-based network is adopted for the fault diagnosis, using the normalized diagnosis variables χ_a, χ_b and χ_c of the current-sensor signals as input. Firstly, two-phase current signals are collected by the sensors installed between the inverter and the motor, respectively. Then, a normalization process is applied to extract suitable features. Finally, the normalized input sensor data [χ_a χ_b χ_c] are put into the BiLSTM network.

The output of the BiLSTM network is a concatenation of the forward and backward hidden states. The final output of the network contains six flags [T_1 T_2 T_3 T_4 T_5 T_6], which represent the healthy or faulty state of each power switch of the inverter that controls the IM. Each flag can take either the value 1 to indicate that the desired power switch is infected, or the value 0 to indicate that the desired switch is healthy. The proposed BILSTM enables us to predict and identify 21 open-circuit faulty states and 1 normal state. The structure of the fault-diagnosis method based on the BiLSTM network is illustrated in Figure 9.

To train the BiLSTM network to work efficiently, the system requires normal and faulty feature data. For this, we generated all possible single and multiple open-circuit fault scenarios. Thirty thousand samples are used as training data for each class of default, with a sampling time of 10^{-4} s. The cost function used in the training process is the root-mean-square error (RMSE).

After many trials ranging from 10 to 100, as shown in Figure 10, the size of the hidden layer of BiLSTM network is set as 100 units to make a tradeoff between accuracy and computation time.

The maximum training epoch is set as 1000 to ensure that the error after training is small enough. The BiLSTM model is trained using the LSTM MATLAB toolbox vR2020b.

The parameters of the BiLSTM models are summarized in Table 1.

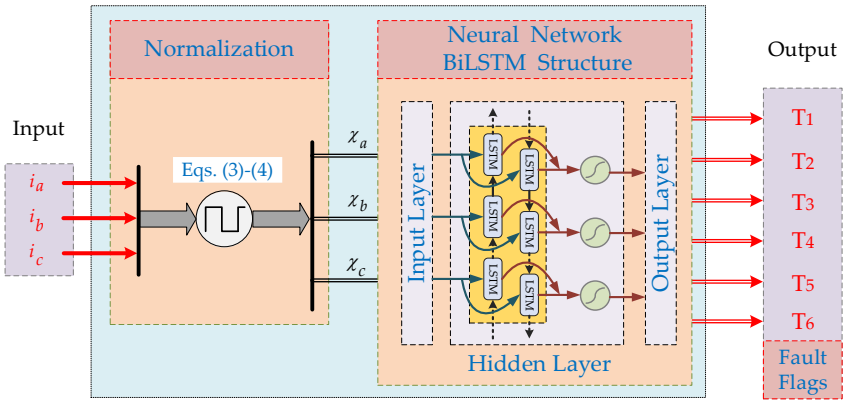

Figure 9. Structure of the fault-diagnosis module based on BiLSTM network.

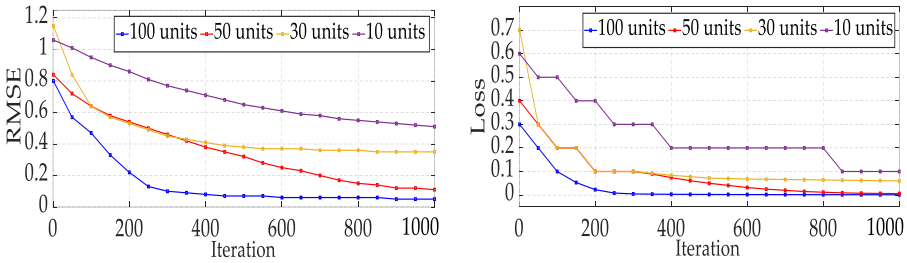

Figure 10. (**a**) Evolution of the RMSE as a function of hidden layer size in training progress of BiLSTM Network, (**b**) Evolution of the Loss as a function of hidden layer size.

Table 1. BiLSTM parameter.

Parameter	Value
Max training epochs	1000
Loss function optimizer (solver)	Adam
Initial learning rate	0.001
Loss function	RMSE
Gradient threshold	0.001
Hidden units	100

The principle of the proposed BiLSTM-based fault-diagnosis method considering the data detailed above is shown in Algorithm 1.

Algorithm 1: BiLSTM-based Fault-Diagnosis Algorithm

Step 1: Data set collection.

– Fault-detection variables [χ_a χ_b χ_c].
– Fault flags [T_1 T_2 T_3 T_4 T_5 T_6].

Step 2: Parameter initialization.
Step 3: Set the BiLSTM model.

– Forward hidden layer output h_t^f: $h_t^f = \sigma(w_x^f X_t + w_x^f h_{t-1}^f + b_h^f)$.
– Backward hidden layer output h_t^b: $h_t^b = \sigma(w_x^b X_t + w_h^b h_{t-1}^b + b_h^b)$.
– The model output y_t: $y_t = w_y^f h_t^f + w_y^b h_t^b + b_y$.

Step 4: Train the BiLSTM model.
Step 5: Return the network model (w, b).
Step 6: Test model. If the evaluation metrics are not satisfactory, then adjust network parameters and go to Step 3.

After training, the performance and efficiency of our network were tested in a situation in which open-circuit switch faults occur simultaneously in T_5 and T_6 at t = 1 s. The simulation results are shown in Figure 11a,b.

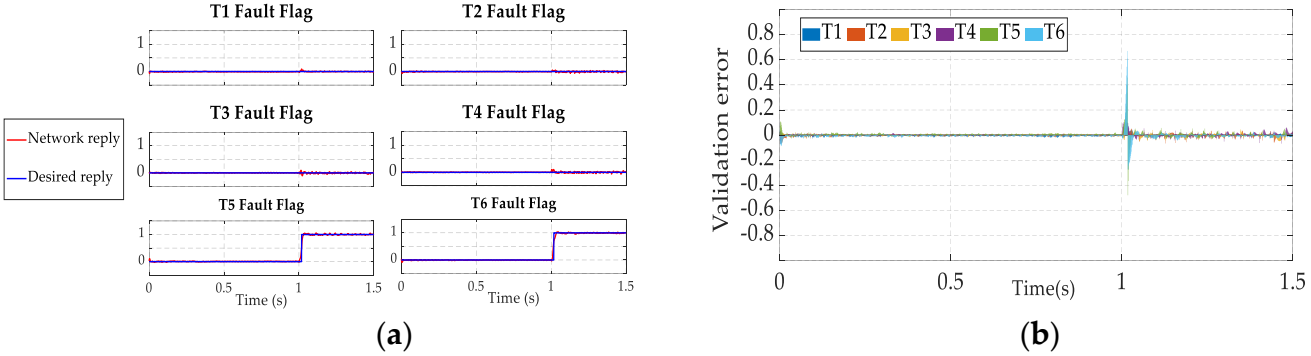

Figure 11. Simulation results: (**a**) Test of BiLSTM Network in the presence of T_5 and T_6 fault, (**b**) Validation error of BiLSTM model.

It can be seen from Figure 11b that the validation error value varies between −0.05 and 0.05, with a little increase when the fault begins to occur (t = 1 s); this result demonstrates the efficiency of the proposed model in the prediction of default class and the time at which the fault occurs.

4. Simulation Results

The performance of the proposed open-switch fault-detection approach is first analyzed through simulations using MATLAB/Simulink Software vR2020b for a variable-speed three-phase induction-motor drive. In this section, the robustness of the proposed method under speed/load-torque variations is studied first. Then, the effectiveness of the proposed approach in detecting single and multiple open-switch faults is presented.

4.1. Robustness under Operating Point Variations

The performances of the proposed fault-diagnosis approach under motor-speed and load-torque variations are presented in Figures 12 and 13, respectively. Figure 12 presents variations in stator current, motor speed, detection variables, and the output of the BiLSTM network ($T_1 \rightarrow T_6$ fault flags) when the motor speed varies from 1200 to 1500 rpm at time t = 1 s with no load. The detection variables maintain the same behavior during steady-state operation as well as during a transient state. Finally, all fault flags remain at low levels, equal to 0. Figure 13 describes the same variables in the case of torque-load change from 0 N·m to 3 N·m at time t = 1 s with motor speed equal to 1000 rpm. Here, again, all fault flags remain at a value of 0, and no false alarm is triggered.

4.2. Open-Switch Fault Detection

In Figure 14, the stator currents for an OC fault in the upper switch T_1 of phase a, with 4 N·m as the load torque and 800 rpm as the rotor speed, are presented. When the open-switch fault of IGBT T_1 is applied at t = 1 s, the positive half-cycle of the current i_a is deleted. Therefore, the lost variable χ_a is a positive sequence and varies between the values −4 and 0, whereas both the other diagnostic variables, χ_b and χ_c, vary between values −3 and 4. Hence, the T_1 fault flag increases instantly to 1 after 4 ms of fault appearance, relevant to 10% of the stator current's fundamental period.

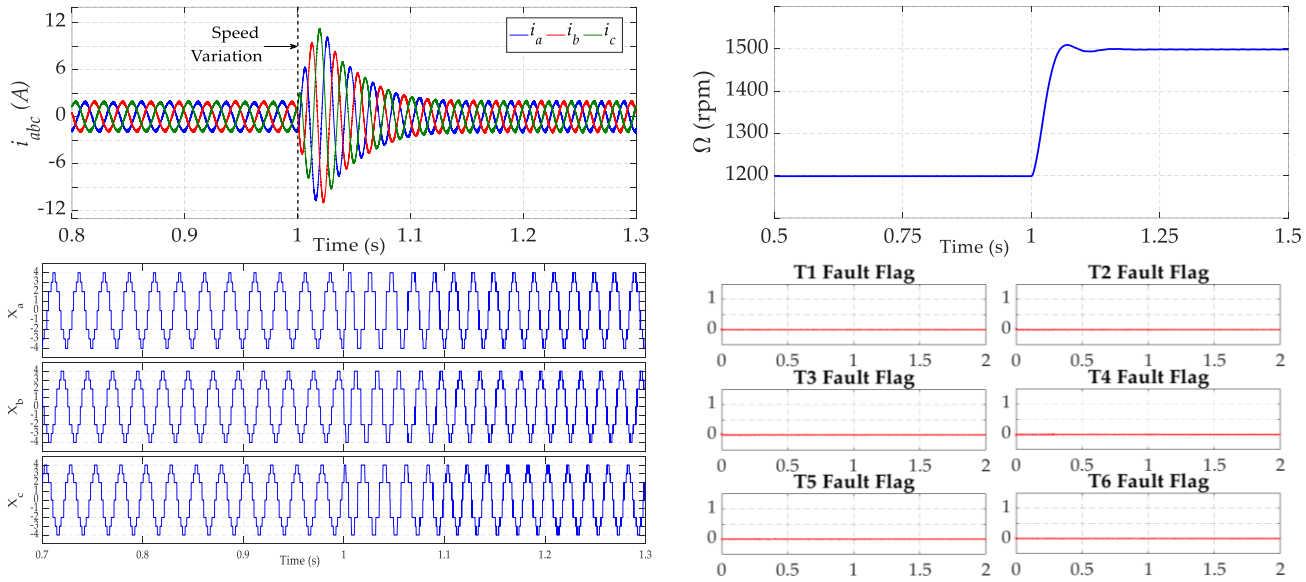

Figure 12. Simulation results for speed variation from 1200 to 1500 rpm without load.

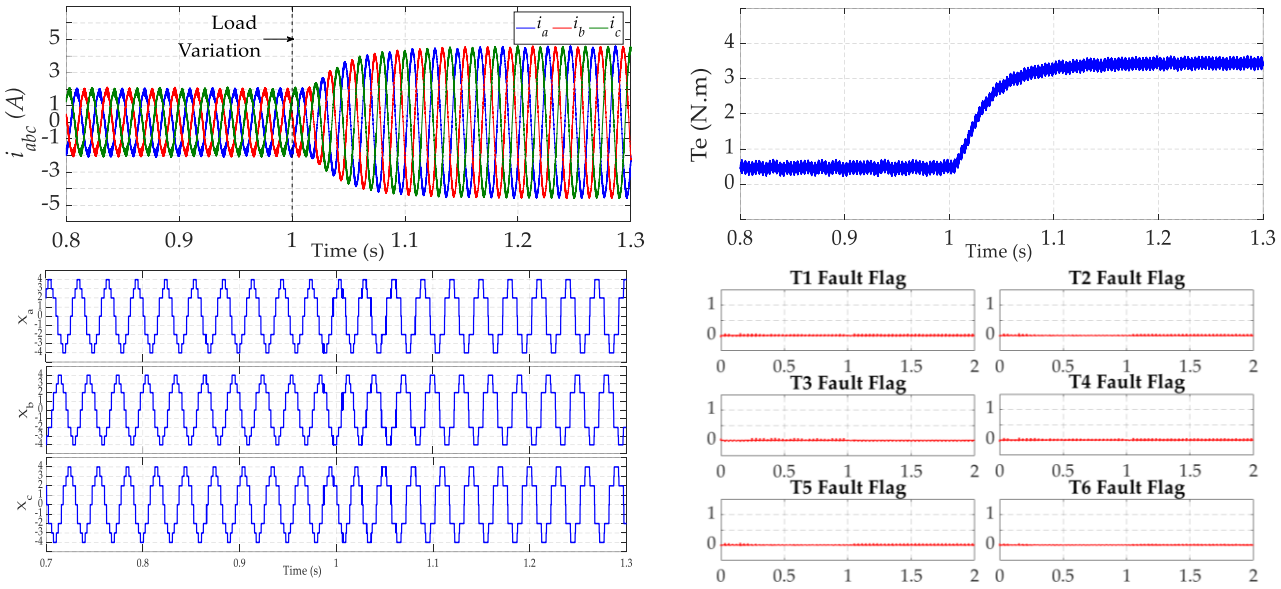

Figure 13. Simulation results for load variation from 0 to 3 N·m under a speed of 1000 rpm.

The performance of the proposed approach relating to the diagnosis of an open-phase fault is shown in Figure 15. Primarily, a single OC fault in power switch T_1 occurred at time t = 1 s, where the motor is running at the speed of 1400 rpm and the load torque is equal to 3 N·m. The faulty power switch is identified when the T_1 fault flag increases to 1 at time t = 1.003 s, equal to 14% of the motor current's fundamental period. At t = 1.5 s, the fault in IGBT T_2 is added, and the behavior of the fault-diagnosis variables automatically changes. Regarding all diagnosis variables in this failure situation (open-phase fault), the diagnosis variable χ_a becomes equal to 0, but the other variables, χ_b and χ_c, take the values of -3 and 3. Then, the open-phase fault is distinguished when both T_1 and T_2 fault flags take the value 1, 4 ms after fault occurrence, equal to 19% of the motor current's fundamental period.

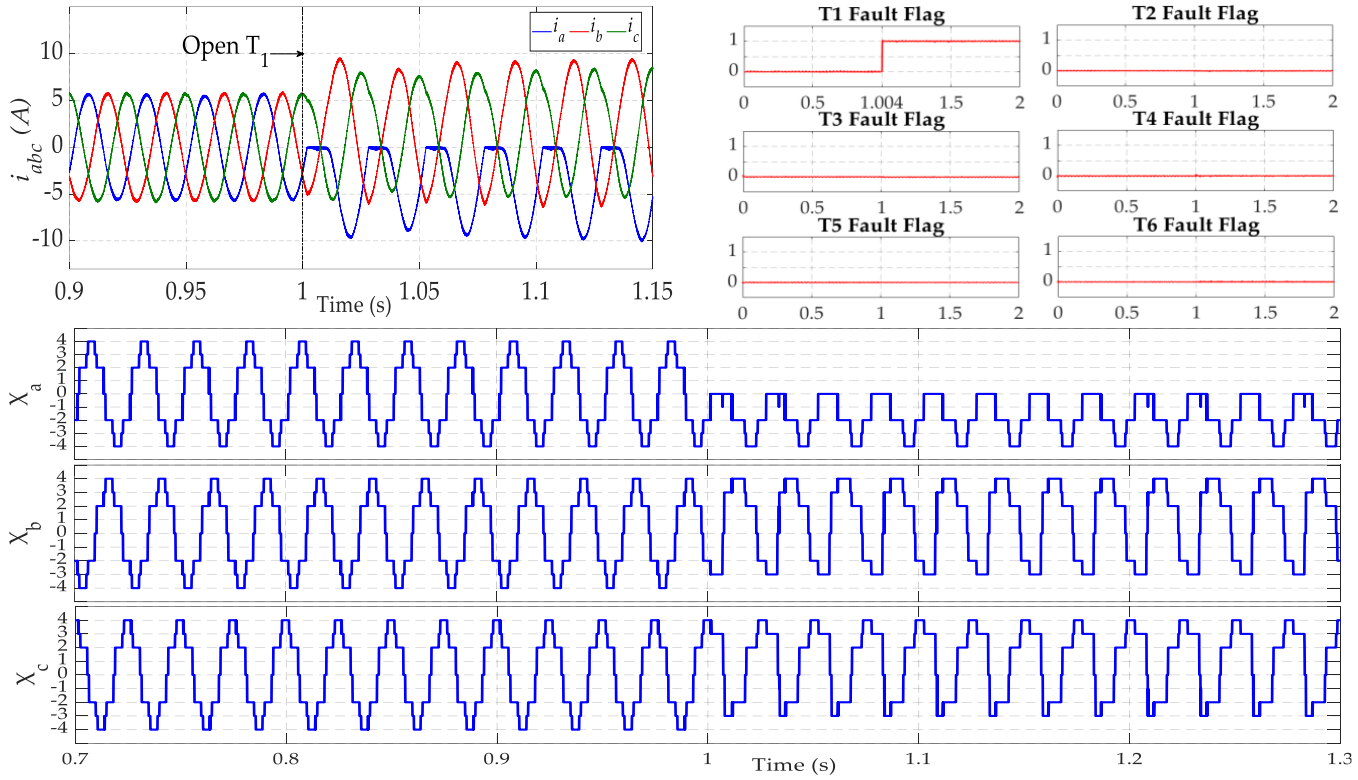

Figure 14. Simulation results for a fault in T_1 under a speed of 800 rpm and a load torque of 4 N·m.

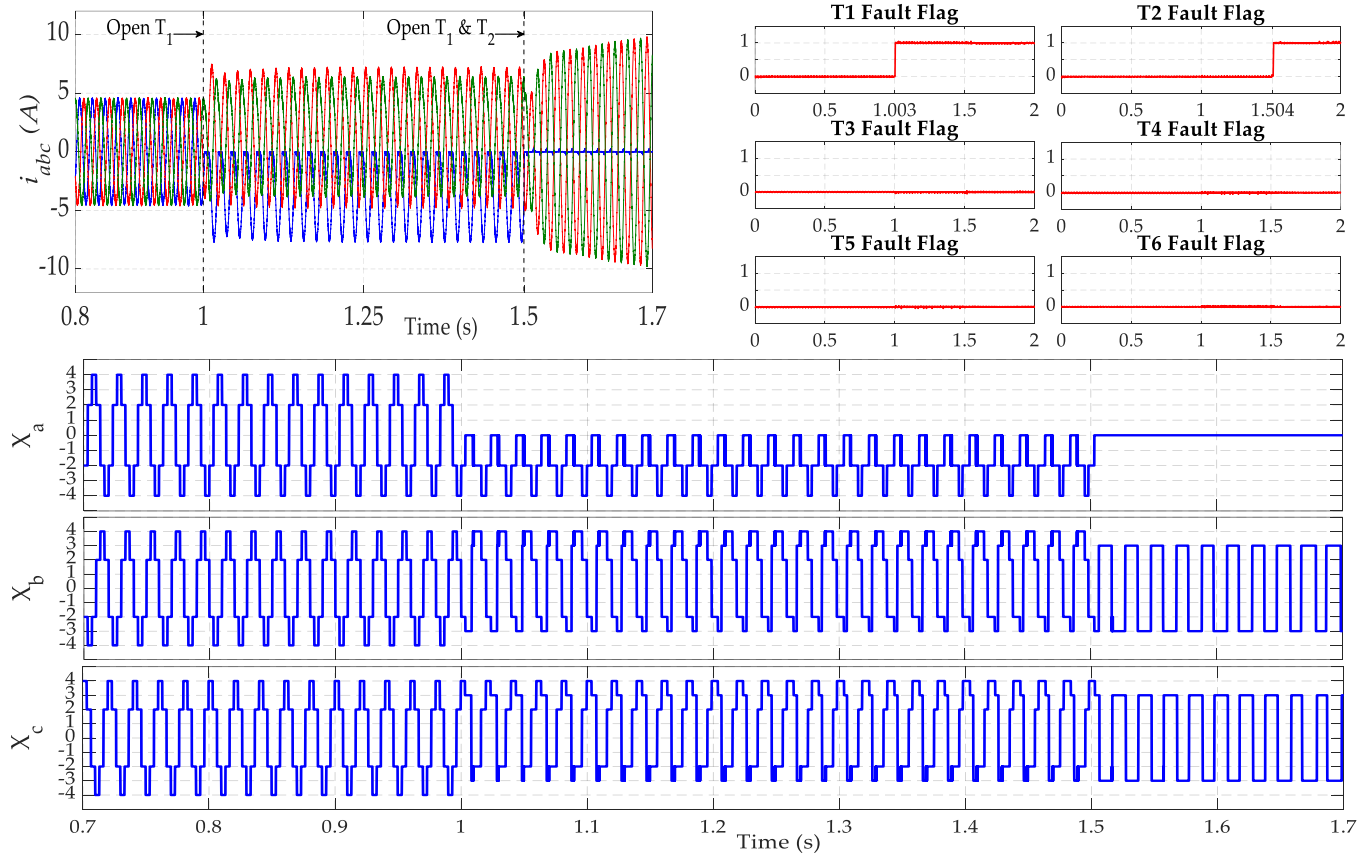

Figure 15. Simulation results for a fault in T_1 and T_2 under a speed of 1400 rpm and a load torque of 3 N·m.

The steady-state performance of the proposed AI approach for both open-switch faults in the VSI is presented in Figure 16. Firstly, an OC fault in IGBT T_1 appears at t = 1 s, under the operating speed of 1200 rpm and with 3 N·m as the load torque. The infected IGBT is localized by switching the T_1 fault-flag value to 1 at t = 1.004 s, with 10% of the fundamental period as a delay. At t = 1.5 s, the second fault in T_4 is added, and the first diagnostic variable χ_a maintains its negative sequence. However, the second diagnostic variable χ_b changes its behavior by losing its negative sequence, varying between 0 and 4, whereas χ_c varies between −3 and 3. For this state, the T_4 fault flag needs 3.5 ms as a time delay to take the value 1, which would denote that an open-circuit fault has occurred in power switch T_4. The detection time of this fault is equal to 8.75% of the current's fundamental period.

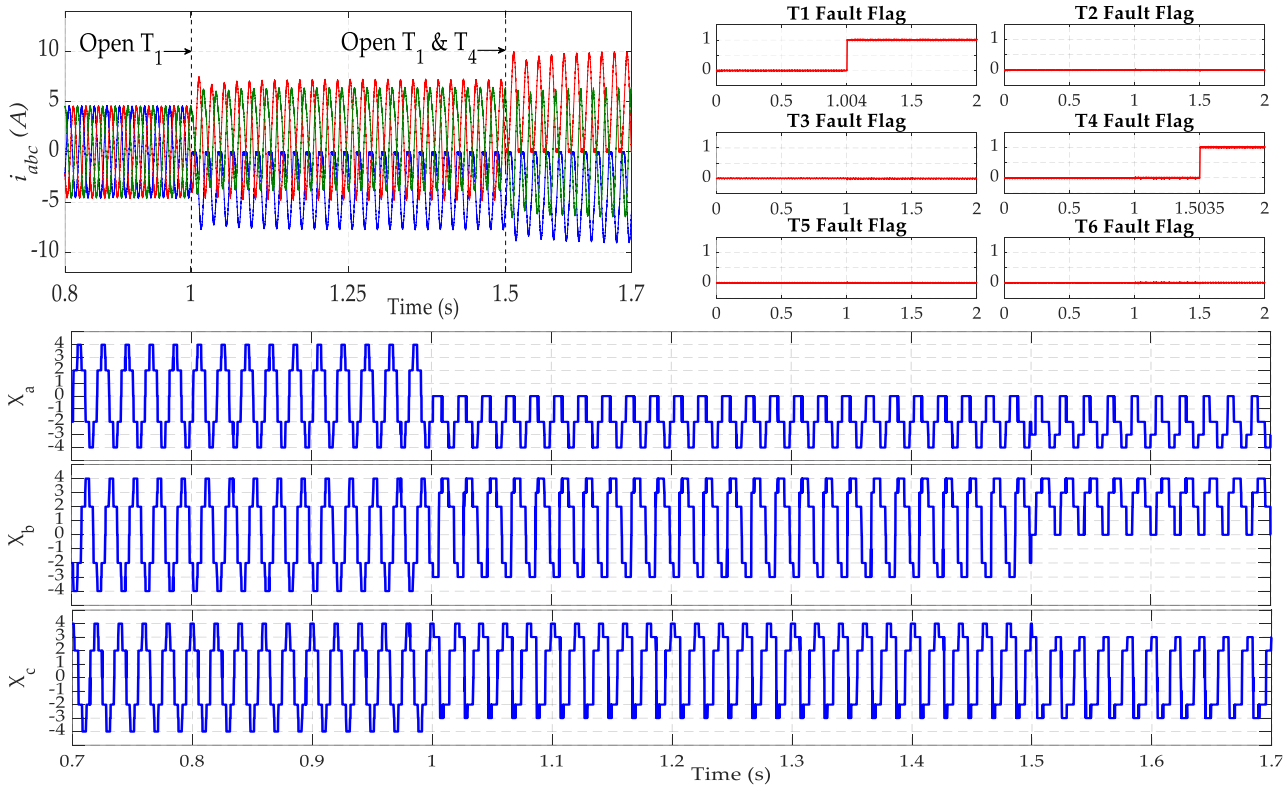

Figure 16. Simulation results for a fault in T_1 and T_4 under a speed of 1200 rpm and a load torque of 3 N·m.

5. Experimental Results

The performances of the proposed open-circuit fault-diagnosis method were examined using a 3 kW induction-motor drive prototype. The experimental test bench, shown in Figure 17, comprises a three-phase voltage source inverter (SEMIKRON), fed by a 3 kW PV array, and an induction motor coupled with a permanent magnet synchronous generator (PMSG). A digital signal processor (DSP-Dspace1104) is used for the motor drive system control. The SEMIKRON inverter is composed of three IGBT modules (SKM50GB12T4) and a 1100µF DC capacitor supporting 750VDC. The switching frequency was set to 5 kHz, and the sampling period was 100 µs. Two Hall-effect current sensors (LEM LA55P) were used for sensing motor-phase currents. A Keithley (DT9834) data acquisition module with a 16-bit resolution analog input and a sample rate of 500 kS/s throughput was used for recording the test results. A fault-gate generator box was used to generate an IGBT opening fault. The idea is to switch the PWM signal input of the gate driver to zero in the fault case. The mechanical load could be established with the help of the PMSG coupled to the PD3 rectifier and a variable resistive load. The OC fault was introduced by removing the gate

command signal of the considered faulty IGBT. The parameters of the IM are shown in Table 2.

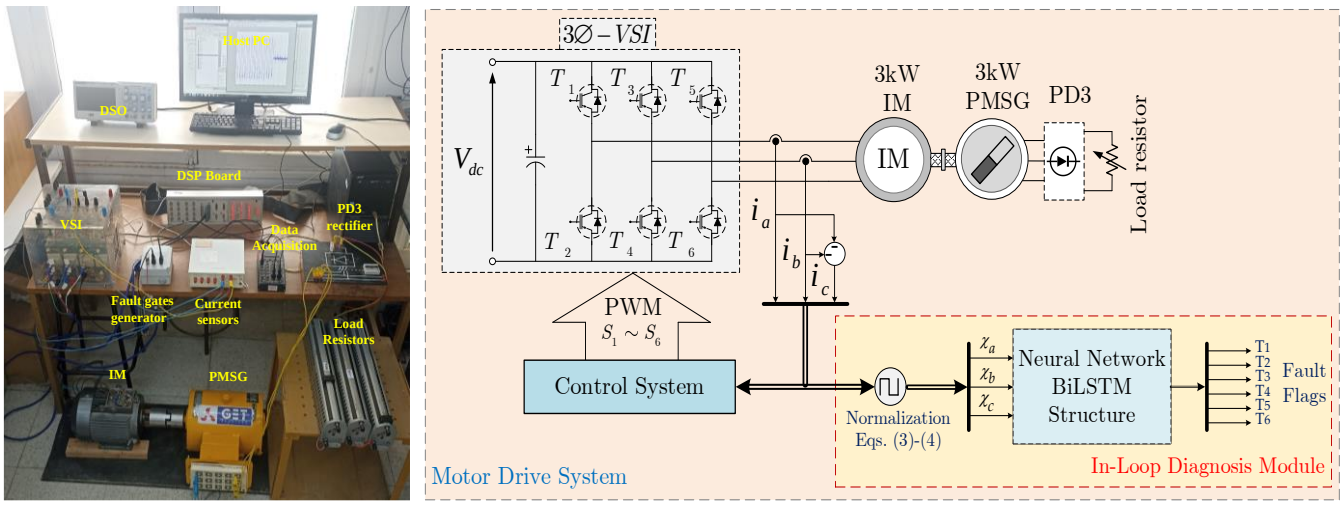

Figure 17. Experimental test bench with the architecture of the complete system.

Table 2. IM parameters.

Parameter	Symbol	Value	Parameter	Symbol	Value
Rated Power	P_a	3000 W	Stator Resistance	R_s	2.26 Ω
Rated Voltage	V	380 V	Rotor Resistance	R_r	1.45 Ω
Rated Current	I_n	6.2 A	Stator Inductance	L_s	0.249 H
Rated Frequency	F	50 Hz	Rotor Inductance	L_r	0.249 H
Rated Speed	Ω	1430 rpm	Mutual Inductance	L_m	0.237 H
Rated Torque	T_e	20 N·m	Moment of Inertia	J	6.84×10^{-3} Kg·m^2
Pair of Poles	P	2	Friction Coefficient	f	3.745×10^{-4} N·m·s/rad

5.1. Robustness under Operating Point Variations

The experimental results, reported in Figure 18, show the time-domain waveforms of the phase currents and the IGBT fault flags used for open-circuit fault diagnosis in the VSI. In this evaluation, a fast transient process was conducted using a speed step from 700 to 1000 rpm under no load for the first test and a rated load torque under 60% for the second test. Figure 19 provides the experimental results when the 3Φ-IM operates at a mechanical rotor speed equal to 1000 rpm. The transient states consist of applying two-step transitions of the load torque to the IM: the rated load torque from 0 to 60% and then the rated load torque from 60% to 0%. For the diagnostic variables, even though transient states are observed, they present the same behavior, which corresponds to a healthy operation mode of the VSI. Regarding the outputs of the BiLSTM network, all fault flags remain at their 0 values. The obtained results confirm the high performance and robustness of the proposed FDI approach under load and speed change.

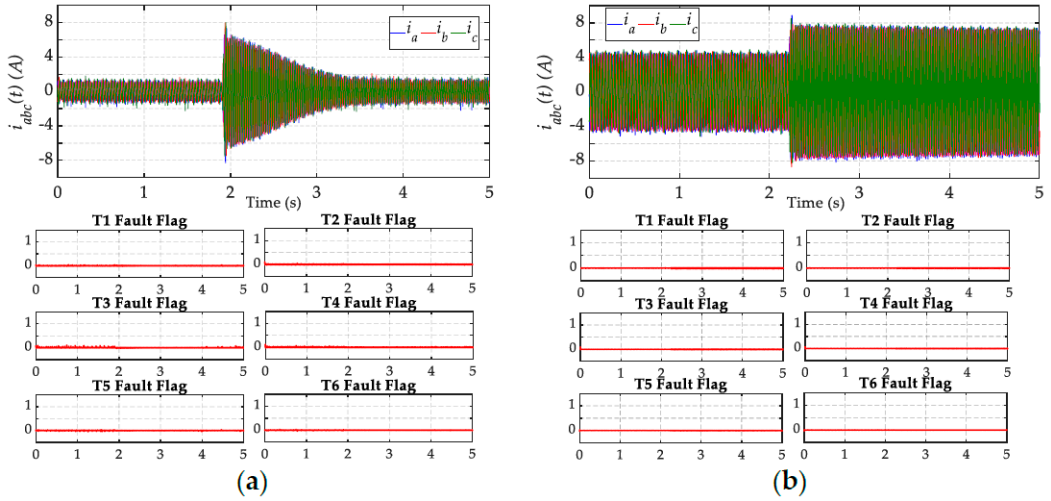

Figure 18. Experimental results for speed variation from 700 to 1000 rpm with: (**a**) no load, (**b**) 60% of rated torque.

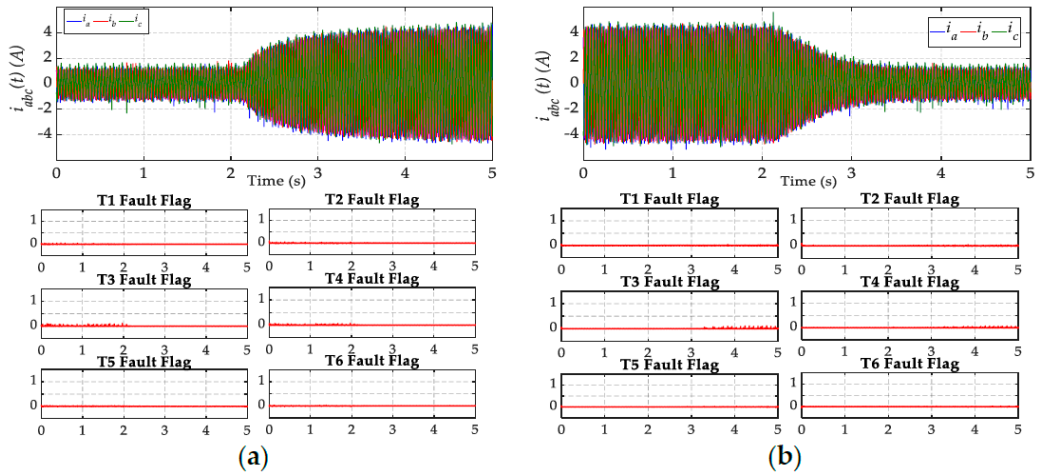

Figure 19. Experimental results for load variation under a speed of 1000 rpm: (**a**) from 0 to 60% of rated torque, (**b**) from 60% to 0% of rated torque.

5.2. Open-Switch Fault Detection

To further examine the practicality of the proposed method, several tests were performed under fault conditions. The first test was conducted when the fault occurred in phase b, resulting from an open-switch fault of IGBT T_4. In this test, the operating point of the motor was fixed, respectively, at Ω = 780 rpm and T_{em} = 50% of rated load torque. The time-domain waveforms of three-phase stator currents; the diagnostic variables χ_{abc}; and the $T_{1\ldots6}$ fault-flag behavior are reported in Figure 20. First, before the introduction of the OC fault, the behavior of the fault-detection variables χ_a, χ_b and χ_c corresponds to the healthy operation of the VSI. At t = 3.605 s, an open-circuit fault occurs in IGBT T_4 of the second inverter leg by fixing its switching signal in the « 0 » state. As a result, the negative half-cycle of the current i_b is cut and is now limited to only flowing in the positive direction, while other currents (i_a and i_c) undergo a light deformation and flow in negative and positive directions. Consequently, the behavior of three diagnostic variables ($\chi_{a,b,c}$) is not yet the same as in the healthy operation mode. Indeed, χ_b loses its negative sequence, varying between 0 and 4, whereas χ_a and χ_c vary between -4 and 3. As a result, the fault flag corresponding to the faulty IGBT T_4 immediately takes the value of 1 at t = 3.609 s, and there is a time delay equal to 12% of the current's fundamental period.

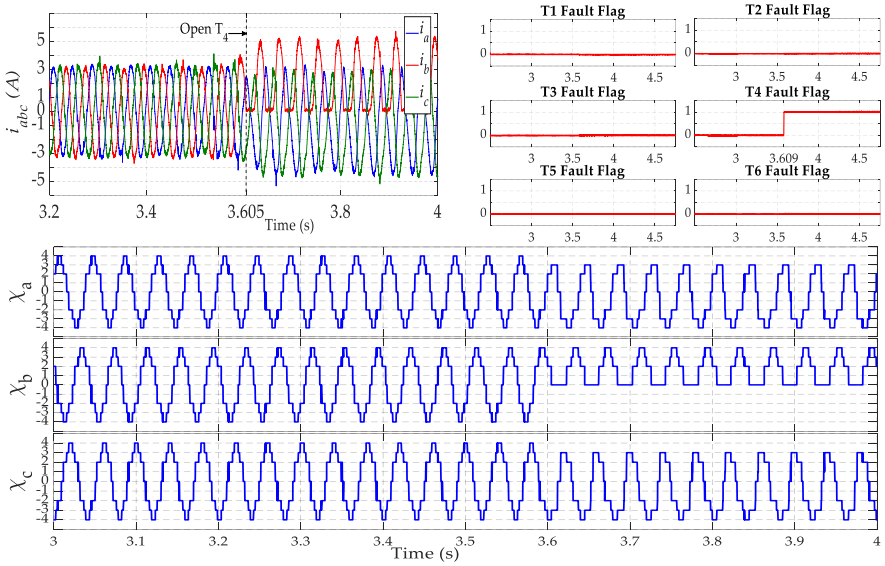

Figure 20. Experimental results for a fault in T_3 under a speed of 780 rpm and 50% of rated torque.

The second test corresponds to an open-phase fault involving two IGBTs in the same inverter leg (T_1 and T_2). Figure 21 presents the experimental results of the output-inverter currents together with the diagnostic variables used for FDI in the VSI and the outputs of the BiLSTM network. However, the motor speed and the load torque are, respectively, fixed at Ω = 990 rpm and T_{em} = 50% of the rated load torque. The fault is introduced into the first inverter leg at t = 1.378 s by keeping the switching signals of both IGBTs simultaneously in the « OFF » state. In this case, current i_a becomes equal to zero over the whole current cycle, while the other currents maintain their sinusoidal shapes but oscillate in phase opposition between -4 A and 4 A. As soon as the fault occurs, the diagnostic variable χ_a takes the value of zero, and the other diagnostic variables χ_b and χ_c are opposite and vary between 3 and -3. As learned in offline conditions, the diagnostic algorithm based on the BiLSTM network decides that the fault is an open phase involving the first inverter leg. As a result, open-phase fault identification is achieved at t = 1.387 s when both T_1 and T_2 fault flags switch from 0 to 1, and there is a time delay equal to 30% of the current's fundamental period.

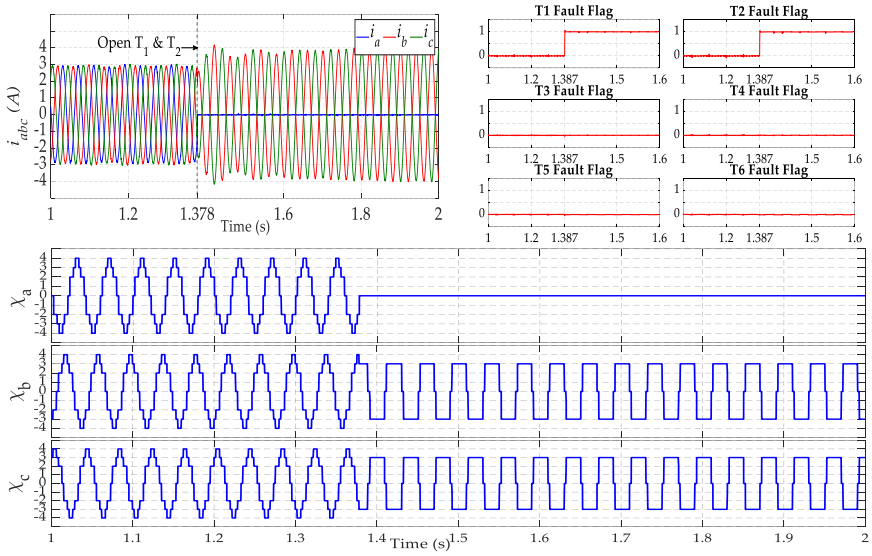

Figure 21. Experimental results for a double fault in T_1 and T_2 under a speed of 990 rpm and 50% of load.

The last test, which presents the performance of the proposed algorithm regarding the diagnosis of a double fault in the power switches T_2 and T_4, is depicted in Figure 22. In this case of faulty condition, the 3Φ-IM runs under a speed of 1000 rpm and no load. The fault is applied between t = 2.54 s and t = 6.4 s. During this time, current i_a loses its negative half-cycle and current i_b loses its positive half-cycle, whereas current i_c is slightly deformed but maintains its sinusoidal form. Immediately, diagnostic variables χ_a and χ_b lose their negative and positive sequences, respectively, while variable χ_c varies between −3 and 3. As a consequence, the FDI approach replies immediately—the T_2 and T_3 fault flags take the value of 1 between times 2.544 s and 6.405 s. The detection time of the fault condition corresponds to 16% of the motor current's fundamental period.

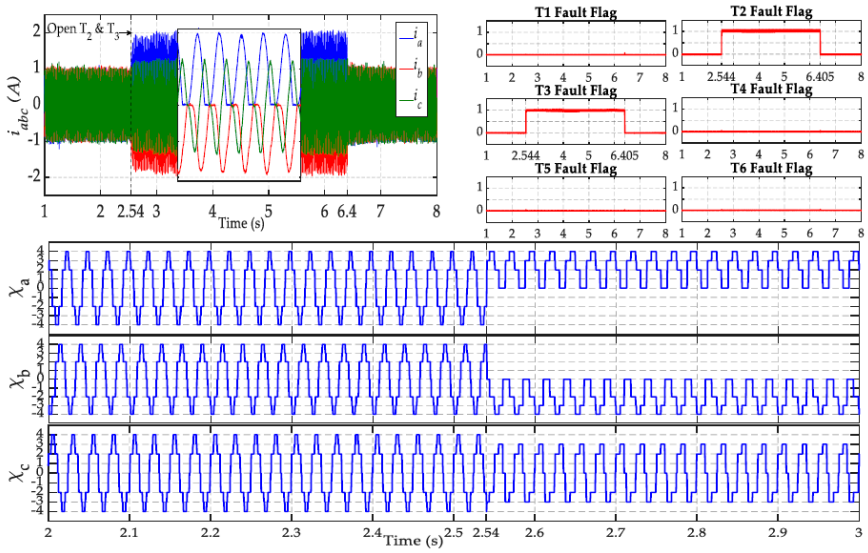

Figure 22. Experimental results for a double fault in T_2 and T_3 under a speed of 1000 rpm and no load.

5.3. Performance Evaluation and Comparison

The proposed fault-diagnosis method is applied to a 3Φ-induction-motor system for certain faults: T_1, T_2, T_3, T_4, T_5, T_6, T_1 and T_2, T_3 and T_4 and T_5 and T_6. About 1500 testing samples of each fault were used to validate the performance of the proposed BiLSTM-based method and other comparison methods, including standard LSTM, stacked LSTM (MLSTM), and feed-forward neural network (FFNN). These network structures are engaged as comparison methods to prove the efficiency and robustness of the proposed method. The FFNN and LSTM are trained with 100 units in 1 hidden layer, while the MLSTM models are trained with 50 units in each hidden layer. The training parameters of the BiLSTM model were considered for the other network structures. The different methods were tested in a situation where an OC fault occurs at t = 0.5 s. Table 3 presents the RMSE, MAE, time detection, and accuracy of each model.

Figure 23 shows MAE evolution in a situation when an open-circuit switch fault happens in T_1 and T_2 at t = 0.5 s. This metric is illustrated for the BiLSTM and the other comparison methods.

Figure 24 shows the RMSE evolution for each fault (T_1, T_2, T_3, T_4, T_5, T_6) in a situation when an open-circuit fault happens in T_1 and T_2 at t = 0.5 s. The RMSE is illustrated for the BiLSTM and the other comparison methods.

According to Table 3, the RMSE and MAE values of the BiLSTM method converge towards 0, which explains its high prediction accuracy in fault detection and identification (98.07%). This percentage is better than the accuracy reported by the FFNN and classic LSTM networks. Moreover, the BiLSTM's detection time of fault conditions varies between 2.5 ms and 6 ms, which corresponds to 12–30% of the motor current's fundamental pe-

riod. Consequently, the BiLSTM approach can identify and predict various fault scenarios accurately and quickly.

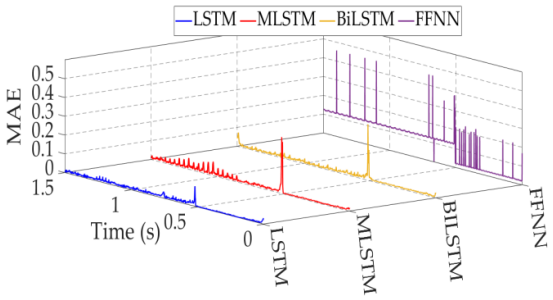

Figure 23. MAE evolution when open-circuit switch fault happens in T_1 and T_2 for the BiLSTM and the other comparison methods.

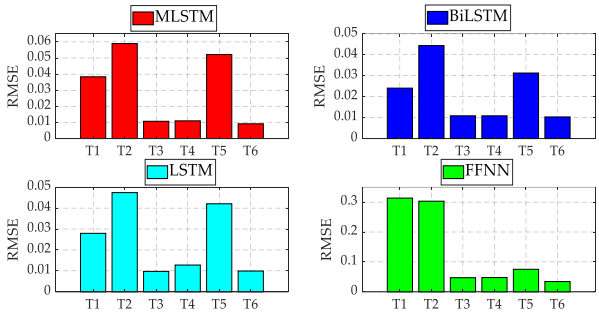

Figure 24. Performance evolution: RMSE evolution for each fault (T_1, T_2, T_3, T_4, T_5, T_6) when an open-circuit switch fault happens in T_1 and T_2 for the BiLSTM and the other comparison methods.

Moreover, appending additional layers for a classic LSTM network does not greatly improve the performance of the detection model since the LSTM and the MLSTM have the same accuracy—97%. However, it increases the calculation time. In addition, there is not a big difference in the fault-detection time, which can reach up to 24 ms.

On the other hand, the FFNN is the fastest for fault detection because the detection time is around 1 ms, but it has the lowest accuracy—48%. To prove the robustness of the BiLSTM network, the proposed method is tested on several faults at different operating points by varying the motor speed and the rated torque. The results are shown in Figures 18–22. In all cases, the method based on BiLSTM ensures the best performance. This again demonstrates the effectiveness and the robustness of the proposed method.

Consequently, the BiLSTM model can be used for effective open-circuit fault detection in a 3Φ-induction-motor-based drive system.

Table 4 presents a comparative analysis of the proposed fault-diagnosis technique, specifically for OC faults, against techniques previously used for IGBT faults, with a particular emphasis on detection time, accuracy, and implementation effort. The detection time is evaluated in relation to the current's fundamental period. The data in Table 4 clearly show that most of the techniques based on signal or/and model approaches present a low detection time that does not exceed the fundamental period for diagnosis, with little implementation effort. On the other hand, the fault-diagnosis techniques based on the artificial intelligence approach present a higher detection time and implementation effort but an accuracy near 100%. Compared to the two types of OC fault-diagnosis techniques, the proposed method based on the BiLSTM neural network demonstrates strong performance across the evaluated parameters. Considering various fault modes, including multiple IGBT open-circuit faults, the tests show that the proposed method balances the diagnostic speed and accuracy well: the fault-detection time is lower than 30% of one current's fundamental period; the accuracy value is equal to 98.08%; and there is a low implementation effort, which outperforms state-of-the-art learning algorithms.

Table 3. Performance evaluation for each method.

Faulty Switch	FFNN				LSTM				MLSTM (3 Layers)				BiLSTM			
	RMSE	MAE	T_d (ms)	Accuracy (%)	RMSE	MAE	T_d (ms)	Accuracy (%)	RMSE	MAE	T_d (ms)	Accuracy (%)	RMSE	MAE	T_d (ms)	Accuracy (%)
T_1	0.2073	0.1268	**1**	32.9996	0.0142	**0.0093**	11.5	97.8281	0.0150	0.0101	11	97.5032	**0.0135**	0.0095	3.45	**98.2613**
T_2	0.2002	0.1241	**1.1**	34.4586	0.0209	**0.0128**	21	96.5231	0.0207	0.0137	23	95.7970	**0.0192**	**0.0128**	5.2	**96.5596**
T_3	0.1915	0.1222	**1**	34.8000	0.0186	0.0116	23	96.5823	0.0174	**0.0094**	24	96.8548	**0.0178**	0.0116	6	**97.3394**
T_4	0.1977	0.1241	**1**	33.5121	0.0160	0.0105	16	97.3179	0.0157	0.0102	13.5	97.5014	**0.0146**	**0.0099**	4.88	**97.9273**
T_5	0.1983	0.1235	**1**	33.8192	0.0167	0.0107	21	97.3560	0.0192	0.0121	24	95.1774	**0.0158**	**0.0098**	2.5	**98.1525**
T_6	0.2061	0.1242	**1**	33.6194	0.0162	0.0102	12	97.4939	0.0149	0.0092	13	97.0993	**0.0132**	**0.0089**	4.02	**97.8641**
T_1 & T_2	0.1369	0.0935	**1**	74.1148	0.0250	0.0109	14	98.5637	0.0300	0.0132	17	98.1124	**0.0220**	**0.0105**	2.57	**98.8193**
T_3 & T_4	0.1242	0.0775	**1**	75.8453	**0.0244**	**0.0112**	24	98.2274	0.0270	0.0126	19	96.8244	0.0253	**0.0109**	4.66	**98.3066**
T_5 & T_6	0.1304	0.0796	**1**	76.2560	0.0302	**0.0092**	10	99.3372	**0.0278**	0.0101	16	99.2203	0.0302	0.0101	3.75	**99.4112**
Mean	0.1769	0.1108	**1.0111**	47.7139	0.0202	0.0107	16.94	97.6922	0.0208	0.0111	17.83	97.1211	**0.019**	**0.0104**	4.11	**98.07**

The bold values represent optimum evaluation metrics.

Table 4. Comparative study with other methods.

Method	Research Plant	Faulty Modes	Detection Parameter	Detection Time *	Accuracy	Implementation Effort
System model-based Sliding-Mode Observer (SMO) [13]	PWM VSI-fed sensorless IM drive	IGBT open-switch fault	Current signals, speed signals and IM model	20%	--	Medium
Output line voltage residuals [17]	IM drive	IGBT open-switch fault	Three-phase currents	5–83%	--	Low
Predictive current errors and Fuzzy Logic approach [23]	PMSM drive	IGBT open-circuit fault	Predictive current errors	12–75%	--	Medium
Online data-driven Random vector functional link (RVFL) [31]	PWM VSI-fed IM drive	IGBT open-circuit fault and current-sensor faults	Three-phase currents and speed signals	110%	98.83%	High
Machine learning-based transferrable data-driven method [33]	Three-phase inverter	IGBT open-circuit fault	Three-phase currents	100%	96.76%	Medium
Wavelet Convolutional Neural Network (WCNN) [36]	PMSM drive	IGBT open-circuit fault	Three-phase currents	1000%	100%	High
Classification of open-circuit faults based on Wavelet Packet and LSTM network [40]	Five-level nested NPP converter	IGBT open- and short-circuit switch faults	Current flying capacitor and voltages switch	120%	99.58%	High
Proposed approach (Prediction of open-circuit faults based on BiLSTM network)	PWM VSI-fed IM drive	IGBT open-circuit fault	Three-phase currents	12–30%	98.08%	Low

*: % of the current's fundamental period.

6. Conclusions

This paper proposes a new BiLSTM-based approach that aims to detect and localize open-circuit faults in three-phase, two-level VSIs for induction-motor drive systems. The proposed method uses only the measured induction-motor stator currents. To keep the proposed fault-diagnosis approach free from load-torque and/or motor-speed variations, an innovative approach is presented for motor-stator current normalization through the sigmoid function. Then, three detection variables—χ_a, χ_b and χ_c—are defined and sent to the BiLSTM network to localize the faulty switch(es). The performances of the proposed algorithm have been analyzed through simulations and experiments and have shown:

i. The robustness of the proposed fault-diagnosis algorithm to load-torque and motor-speed variations, and all switches' fault flags remain at their respective low levels.
ii. The accuracy and capability of the proposed algorithm to diagnose single and multiple open-circuit power-switch faults. Moreover, the detection time is acceptable since it is less than the stator current's period.

The proposed work provides evidence of practical viability through extensive simulations and experimental results, demonstrating real-world applicability and robustness. Therefore, the proposed work represents a more promising and effective solution for the fault diagnosis of single and multiple open-circuit faults without extra hardware for three-phase electric speed drives.

Our team's next step is to investigate the ability of the proposed method to detect current-sensor faults and to discriminate them from open-circuit faults.

Author Contributions: Conceptualization, B.G.; methodology, S.K.E.K.; formal analysis, A.B.R. and S.K.E.K.; investigation, H.M.; resources, S.K.E.K.; writing—original draft preparation, B.G. and H.M.; writing—review and editing, A.B.R. and S.K.E.K.; supervision, S.K.E.K.; project administration, A.B.R. and S.K.E.K. All authors have read and agreed to the published version of the manuscript.

Funding: This work was supported by the Tunisian Ministry of Higher Education and Research under Grant LSE–ENIT-LR 11 ES15.

Data Availability Statement: Data are contained within the article.

Acknowledgments: The authors are grateful for the support from the Tunisian Ministry of Higher Education and Research.

Conflicts of Interest: The authors declare no conflicts of interest.

References

1. Yepes, A.-G.; Lopez, O.; Gonzalez-Pietro, I.; Duran, M.-J.; Doval-Gandoy, J. A Comprehensive Survey on Fault Tolerance in Multiphase AC Drives, Part 1: General Overview Considering Multiple Fault Types. *Machines* **2022**, *10*, 208. [CrossRef]
2. Yepes, A.-G.; Lopez, O.; Gonzalez-Pietro, I.; Duran, M.-J.; Doval-Gandoy, J. A Comprehensive Survey on Fault Tolerance in Multiphase AC Drives, Part 2: Phase and Switch Open-Circuit Faults. *Machines* **2022**, *10*, 221. [CrossRef]
3. Lu, B.; Sharma, S. A literature review of IGBT fault diagnostic and protection methods for power inverters. *IEEE Trans. Ind. Appl.* **2009**, *45*, 1770–1777.
4. Tang, H.; Weili, L.; Zhigang, W. Influence of Inverter Open Circuit Fault on Multiple Physical Quantities in the PMSM. *IEEE Trans. Power Electron.* **2022**, *38*, 901–916. [CrossRef]
5. Zhang, Z.; Hu, Y.; Luo, G.; Gong, C.; Liu, X.; Chen, S. An Embedded Fault-Tolerant Control Method for Single Open-Switch Faults in Standard PMSM Drives. *IEEE Trans. Power Electron.* **2022**, *37*, 8476–8487. [CrossRef]
6. Pires, V.F.; Cordeiro, A.; Foito, D.; Pires, A.J. Fault-Tolerant Multilevel Converter to Feed a Switched Reluctance Machine. *Machines* **2022**, *10*, 35. [CrossRef]
7. Choi, U.T.; Blaabjerg, F.; Lee, K.B. Study and handling methods of power IGBT module failures in power electronic converter systems. *IEEE Trans. Power Electron.* **2015**, *30*, 2517–2533. [CrossRef]
8. Orlowska-Kowalska, T.; Wolkiewicz, M.; Pietrzak, P.; Skowron, M.; Ewert, P.; Tarchała, G.; Krzysztofiak, M.; Kowalski, C.T. Fault diagnosis and fault-tolerant control of PMSM drives–state of the art and future challenges. *IEEE Access* **2022**, *10*, 59979–60024. [CrossRef]
9. Jlassi, I.; Estima, J.O.; El Khil, S.K.; Bellaaj, N.B.; Cardoso, A.J.M. Multiple open-circuit faults diagnosis in back-to-back converters of PMSG drives for wind turbine systems. *IEEE Trans. Power Electron.* **2015**, *30*, 2689–2702. [CrossRef]

10. Jlassi, I.; Estima, J.O.; El Khil, S.K.; Bellaaj, N.B.; Cardoso, A.J.M. A Robust observer-based method for IGBTs and current sensors fault diagnosis in voltage-source inverters of PMSM drives. *IEEE Trans. Ind. Appl.* **2017**, *53*, 2894–2905. [CrossRef]
11. Xu, S.; Huang, W.; Wang, H.; Zheng, W.; Wang, J.; Chai, Y.; Ma, M. A Simultaneous Diagnosis Method for Power Switch and Current Sensor Faults in Grid-Connected Three-Level NPC Inverters. *IEEE Trans. Power Electron.* **2023**, *38*, 1104–1118. [CrossRef]
12. AN, Q.-T.; Sun, L.; Sun, L.-Z. Current residual vector-based open-switch fault diagnosis of inverters in PMSM drive systems. *IEEE Trans. Power Electron.* **2015**, *30*, 2814–2827. [CrossRef]
13. Maamouri, R.; Trabelsi, M.; Boussek, M.; M'Sahli, F. Mixed model-based and signal-based approach for open-switches fault diagnostic in sensorless speed vector-controlled induction motor drive using sliding mode observer. *IET Power Electron.* **2019**, *12*, 1149–1159. [CrossRef]
14. Zhou, X.; Sun, J.; Cui, P.; Lu, Y.; Lu, M.; Yu, Y. A Fast and Robust Open-Switch Fault Diagnosis Method for Variable-Speed PMSM System. *IEEE Trans. Power Electron.* **2020**, *36*, 2598–2610. [CrossRef]
15. Hu, K.; Liu, Z.; Tasiu, I.; Chen, T. Fault Diagnosis and Tolerance with Low Torque Ripple for Open-Switch Fault of IM Drives. *IEEE Trans. Transp. Electrif.* **2020**, *15*, 133–146. [CrossRef]
16. Freire, N.M.A.; Estima, J.O.; Cardoso, A.J.M. A voltage-based approach without extra hardware for open-circuit fault diagnosis in close-loop PWM AC regenerative drives. *IEEE Trans. Ind. Electron.* **2014**, *61*, 4960–4970. [CrossRef]
17. Cheng, Y.; Sun, Y.; Li, X.; Hanbing, D.; Lin, J.; Su, M. Active Common-Mode Voltage-Based Open-Switch Fault Diagnosis of Inverters in IM-Drive Systems. *IEEE Trans. Ind. Electron.* **2020**, *68*, 103–115. [CrossRef]
18. Li, Z.; Ma, H.; Bai, Z.; Wang, Y.; Wang, B. Fast transistor open circuit faults diagnosis in grid tied three phase VSIs based on average bridge arm pole to pole voltages and error adaptive thresholds. *IEEE Trans. Power Electron.* **2018**, *33*, 8040–8051. [CrossRef]
19. Li, Z.; Wheeler, P.; Watson, A.J.; Costabeber, A.; Wang, B.; Ren, Y.; Bai, Z.; Ma, H. A Fast Diagnosis Method for Both IGBT Faults and Current Sensor Faults in Grid-Tied Three-Phase Inverters with Two Current Sensors. *IEEE Trans. Power Electron.* **2020**, *35*, 5267–5278. [CrossRef]
20. Manikandan, R.; Selvaraj, R.; Singh, R.R. Voltage Signature based Open Circuit Switch Fault Diagnosis Strategy for IM Drives with MPC. *IEEE Trans. Ind. Appl.* **2023**, *59*, 6780–6791. [CrossRef]
21. Diao, N.; Zhang, Y.; Sun, X.; Song, C.; Wang, W.; Zhang, H. A Real-Time Open-Circuit Fault Diagnosis Method Based on Hybrid Model Flux Observer for Voltage-Source-Inverter Fed Sensorless Vector Controlled Drives. *IEEE Trans. Power Electron.* **2023**, *38*, 2539–2551. [CrossRef]
22. Hang, J.; Wu, H.; Zhang, J.; Ding, S.; Huang, Y.; Hua, W. Cost Function-based Open-Phase Fault Diagnosis for PMSM Drive System with Model Predictive Current Control. *IEEE Trans. Power Electron.* **2021**, *36*, 2574–2583. [CrossRef]
23. Gmati, B.; Jlassi, I.; Khojet El Khil, S.; Cardoso, A.J.M. Open-switch fault diagnosis in voltage source inverters of PMSM drives using predictive current errors and fuzzy logic approach. *IET Power Electron.* **2021**, *14*, 1059–1072. [CrossRef]
24. Zhang, Y.; Mao, Y.; Wang, X.; Wang, Z.; Xiao, D.; Gaoliang, F. Current Prediction Based Fast Diagnosis of Electrical Faults in PMSM Drives. *IEEE Trans. Transp. Electrif.* **2022**, *8*, 4622–4632. [CrossRef]
25. Huang, W.; Du, J.; Hua, W.; Lu, W.; Bi, K.; Zhu, Y.; Fan, Q. Current-based open-circuit fault diagnosis for PMSM drives with model predictive control. *IEEE Trans. Power Electron.* **2021**, *36*, 10695–10704. [CrossRef]
26. Yan, H.; Xu, Y.; Zou, J.; Fang, Y.; Cai, F. A novel open-circuit fault diagnosis method for voltage source inverters with a single current sensor. *IEEE Trans. Power Electron.* **2018**, *33*, 8775–8786. [CrossRef]
27. Khojet El Khil, S.; Jlassi, I.; Cardoso, A.J.M.; Estima, J.O.; Bellaaj, N.B. Diagnosis of open-switch and current sensor faults in PMSM drives through stator current analysis. *IEEE Trans. Ind. Appl.* **2019**, *55*, 5925–5937. [CrossRef]
28. Estima, J.O.; Cardoso, A.J.M. A new algorithm for real-time multiple open-circuit fault diagnosis in voltage-fed PWM motor drives by the reference current errors. *IEEE Trans. Ind. Electron.* **2013**, *60*, 3496–3505. [CrossRef]
29. Cui, R.; Yu, S.; Li, S. Open-Switch Fault Detection Based on Open-Winding Five-Phase Fault-Tolerant Permanent-Magnet Motor Drives. *Machines* **2022**, *10*, 829. [CrossRef]
30. Abdelkader, R.; Cherif, B.D.E.; Bendiababdella, A.; Kaddour, A. An Open-Circuit Faults Diagnosis Approach for Three-Phase Inverters Based on an Improved Variational Mode Decomposition, Correlation Coefficients, and Statistical Indicators. *IEEE Trans. Instrum. Meas.* **2022**, *71*, 1–9. [CrossRef]
31. Gou, B.; Xu, Y.; Xia, Y.; Qingli, D.; Ge, X. An Online Data-driven Method for Simultaneous Diagnosis of IGBT and Current Sensor Fault of 3-Phase PWM Inverter in Induction Motor Drives. *IEEE Trans. Power Electron.* **2020**, *35*, 13281–13294. [CrossRef]
32. Cai, B.; Zhao, Y.; Liu, H.; Xie, M. A data-driven fault diagnosis methodology in three-phase inverters for PMSM drive systems. *IEEE Trans. Power Electron.* **2017**, *32*, 5590–5600. [CrossRef]
33. Xia, Y.; Xu, Y. A transferrable data-driven method for IGBT open-circuit fault diagnosis in three-phase inverters. *IEEE Trans. Power Electron.* **2021**, *36*, 13478–13488. [CrossRef]
34. Li, Z.; Gao, Y.; Zhang, X.; Wang, B.; Ma, H. A Model-Data-Hybrid-Driven Diagnosis Method for Open-Switch Faults in Power Converters. *IEEE Trans. Power Electron.* **2021**, *36*, 4965–4970. [CrossRef]
35. Gonzalez-Jimenez, D.; del-Olmo, J.; Poza, J.; Garramiola, F.; Sarasola, I. Machine learning-based fault detection and diagnosis of faulty power connections of induction machines. *Energies* **2021**, *14*, 4886. [CrossRef]
36. Hang, J.; Shu, X.; Ding, S.; Huang, Y. Robust Open-Circuit Fault Diagnosis for PMSM Drives Using Wavelet Convolutional Neural Network with Small Samples of Normalized Current Vector Trajectory Graph. *IEEE Trans. Ind. Electron.* **2023**, *70*, 7653–7663. [CrossRef]

37. Jin, L.; Mao, Y.; Wang, X.; Lu, L.; Wang, Z. Online Data-Driven Fault Diagnosis of Dual Three-Phase PMSM Drives Considering Limited Labeled Samples. *IEEE Trans. Ind. Electron.* **2023**. [CrossRef]
38. Xue, Z.Y.; Xiahou, K.S.; Li, M.S.; Ji, T.Y.; Wu, Q.H. Diagnosis of Multiple Open-Circuit Switch Faults Based on Long Short-Term Memory Network for DFIG-Based Wind Turbine Systems. *IEEE Trans. Emerg. Sel. Top. Power Electron.* **2020**, *8*, 2600–2610. [CrossRef]
39. Han, Y.; Qi, W.; Ding, N.; Geng, Z. Short-time wavelet entropy integrating improved LSTM for fault diagnosis of modular multilevel converter. *IEEE Trans. Cybern.* **2021**, *52*, 7504–7512. [CrossRef]
40. Ye, S.; Jiang, J.; Junjie, L.; Liu, Y.; Zhou, Z.; Liu, C. Fault Diagnosis and Tolerance Control of Five-Level Nested NPP Converter Using Wavelet Packet and LSTM. *IEEE Trans. Power Electron.* **2020**, *35*, 1907–1921. [CrossRef]
41. Wang, Q.; Yu, Y.; Ahmed, H.O.; Darwish, M.; Nandi, A.K. Open-Circuit Fault Detection and Classification of Modular Multilevel Converters in High Voltage Direct Current Systems (MMC-HVDC) with Long Short-Term Memory (LSTM) Method. *Sensors* **2021**, *21*, 4159. [CrossRef]
42. Kaplan, H.; Tehrani, K.; Jamshidi, M. A Fault Diagnosis Design Based on Deep Learning Approach for Electric Vehicle Applications. *Energies* **2021**, *14*, 6599. [CrossRef]
43. Li, D.; Zhang, Z.; Liu, P.; Wang, Z.; Zhang, L. Battery Fault Diagnosis for Electric Vehicles Based on Voltage Abnormality by Combining the Long Short-Term Memory Neural Network and the Equivalent Circuit Model. *IEEE Trans. Power Electron.* **2021**, *36*, 1303–1315. [CrossRef]
44. Husari, F.; Seshadrinath, J. Stator Turn Fault Diagnosis and Severity Assessment in Converter Fed Induction Motor Using Flat Diagnosis Structure Based on Deep Learning Approach. *IEEE J. Emerg. Sel. Top. Power Electron.* **2023**, *11*, 5649–5657. [CrossRef]
45. Guo, J.; Lao, Z.; Hou, M.; Li, C.; Zhang, S. Mechanical fault time series prediction by using EFMSAE-LSTM neural network. *Measurement* **2021**, *173*, 108566. [CrossRef]
46. Saadi, M.N.; Bouteraa, N.; Redjati, A.; Boughazi, M. A novel method for bearing fault diagnosis based on BiLSTM neural networks. *Int. J. Adv. Manuf. Technol.* **2023**, *125*, 1477–1492.
47. Guo, Y.; Mao, J.; Zhao, M. Rolling Bearing Fault Diagnosis Method Based on Attention CNN and BiLSTM Network. *Neural Process. Lett.* **2023**, *55*, 3377–3410. [CrossRef]
48. Wang, J.; Guo, J.; Wang, L.; Yang, Y.; Wang, Z.; Wang, R. A hybrid intelligent rolling bearing fault diagnosis method combining WKN-BiLSTM and attention mechanism. *Meas. Sci. Technol.* **2023**, *34*, 085106. [CrossRef]
49. Zhang, Y.; Zhang, S.; Jia, X.; Zhang, X.; Tian, W. A novel integrated fault diagnosis method of chemical processes based on deep learning and information propagation hysteresis analysis. *J. Taiwan Inst. Chem. Eng.* **2023**, *142*, 104676. [CrossRef]
50. Xu, Z.; Mei, X.; Wang, X.; Yue, M.; Jin, J.; Yang, Y.; Li, C. Fault diagnosis of wind turbine bearing using a multi-scale convolutional neural network with bidirectional long short term memory and weighted majority voting for multi-sensors. *Renew. Energy* **2022**, *182*, 615–626. [CrossRef]
51. Yan, X.; Guan, T.; Fan, K.; Sun, Q. Novel double layer BiLSTM minor soft fault detection for sensors in air conditioning system with KPCA reducing dimensions. *J. Build. Eng.* **2021**, *44*, 102950. [CrossRef]
52. Zheng, X.; Chen, W. An attention-based Bi-LSTM method for visual object classification via EEG. *Biomed. Signal Process Contr.* **2021**, *63*, 102174. [CrossRef]